

GENERALIZED CONSISTENCY TRAJECTORY MODELS FOR IMAGE MANIPULATION

Beomsu Kim*
KAIST

Jaemin Kim*
KAIST

Jeongsol Kim
KAIST

Jong Chul Ye
KAIST

ABSTRACT

Diffusion models (DMs) excel in unconditional generation, as well as on applications such as image editing and restoration. The success of DMs lies in the iterative nature of diffusion: diffusion breaks down the complex process of mapping noise to data into a sequence of simple denoising tasks. Moreover, we are able to exert fine-grained control over the generation process by injecting guidance terms into each denoising step. However, the iterative process is also computationally intensive, often taking from tens up to thousands of function evaluations. Although consistency trajectory models (CTMs) enable traversal between any time points along the probability flow ODE (PFODE) and score inference with a single function evaluation, CTMs only allow translation from Gaussian noise to data. This work aims to unlock the full potential of CTMs by proposing generalized CTMs (GCTMs), which translate between arbitrary distributions via ODEs. We discuss the design space of GCTMs and demonstrate their efficacy in various image manipulation tasks such as image-to-image translation, restoration, and editing.

1 INTRODUCTION

Diffusion-based generative models (DMs) learn the scores of noise-perturbed data distributions, which can be used to translate samples between two distributions by numerically integrating an SDE or a probability flow ODE (PFODE) (Ho et al., 2020; Dhariwal & Nichol, 2021; Song et al., 2020). They have achieved remarkable progress over recent years, even surpassing well-known generative models such as Generative Adversarial Networks (GANs) (Goodfellow et al., 2020) or Variational Autoencoders (VAEs) (Kingma & Welling, 2013) in terms of sample quality. Moreover, diffusion models have found wide application in areas such as image-to-image translation (Saharia et al., 2022), image restoration (Chung et al., 2022; 2023), image editing (Meng et al., 2022), etc.

The success of DMs can largely be attributed to the iterative nature of diffusion, arising from its foundation on differential equations – multi-step generation grants high-quality image synthesis by breaking down the complex process of mapping noise to data into a composition of simple denoising steps. We are also able to exert fine-grained control over the generation process by injecting minute guidance terms into each step (Chung et al., 2022; Ho & Salimans, 2022). Indeed, guidance is an underlying principle behind numerous diffusion-based image editing and restoration algorithms.

However, its iterative nature is also a curse, as diffusion inference often demands from tens to thousands of number of neural function evaluations (NFEs) per sample, rendering practical usage difficult. Consequently, there is now a large body of works on improving the inference speed of DMs. Among them, distillation refers to methods which train a neural network to translate samples along PFODE trajectories generated by a pre-trained teacher DM in one or two NFEs. Representative distillation methods include progressive distillation (PD) (Salimans & Ho, 2022), consistency models (CMs) (Song et al., 2023), and consistency trajectory models (CTMs) (Kim et al., 2024b).

In contrast to PD or CMs which only allow traversal to the terminal point of the PFODE, CTMs enable traversal between any pair of time points along the PFODE as well as score inference, all in a single inference step. Thus, in theory, CTMs are more amenable to guidance, and are applicable to a wider variety of downstream image manipulation tasks. Yet, there is a lack of works exploring the effectiveness of CTMs in such context.

In this work, we take a step towards unlocking the full potential of CTMs. To this end, we first propose generalized CTMs (GCTMs) which generalize the theoretical framework behind CTMs with

*Equal Contribution

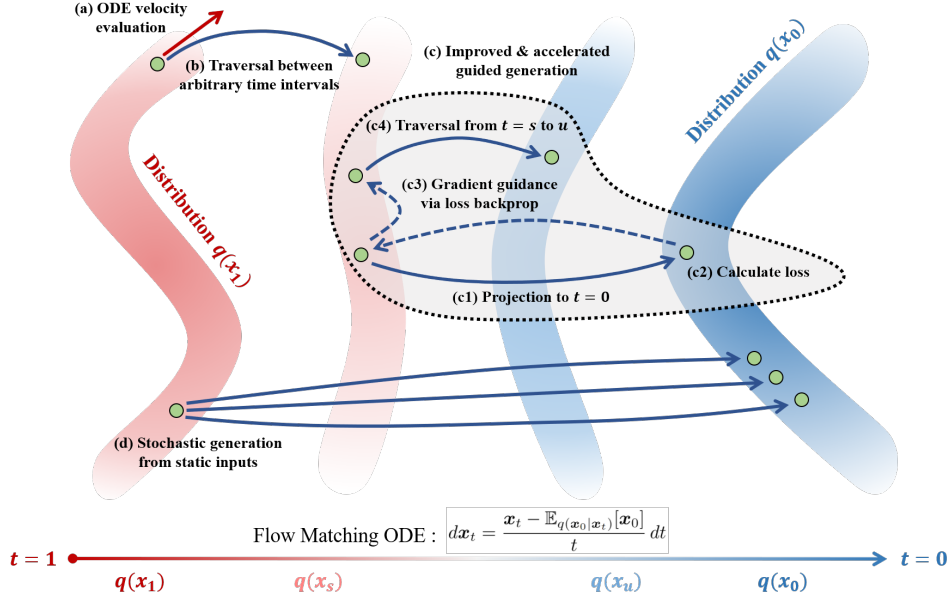


Figure 1: **An illustration of GCTM and its applications – solid arrows can be implemented by a single forward pass of the GCTM network.** GCTMs learn to traverse the Flow Matching ODE which is capable of *interpolating two arbitrary distributions* $q(x_0)$ and $q(x_1)$. GCTMs allow (a) one-step inference of ODE velocity, (b) one-step traversal between arbitrary time intervals of the ODE, (c) improved gradient-guidance by using exact posterior sample instead of posterior mean, and (d) one-step generation of varying outputs x_0 given a fixed input x_1 .

Flow Matching (Lipman et al., 2023) to enable translation between *two arbitrary distributions*. Next, we discuss the design space of GCTMs, and how each design choice influences the downstream task performance. Finally, we demonstrate the power of GCTMs on a variety of image manipulation tasks. Specifically, our contributions can be summarized as follows.

- **Generalization of theory.** We propose GCTMs, which uses conditional flow matching theory to enable one-step translation between two arbitrary distributions (Theorem 1). This stands in contrast to CTMs, which is only able to learn PFODEs from Gaussian to data. In fact, we prove CTM is a special case of GCTM when one side is Gaussian (Theorem 2).
- **Elucidation of design space.** We clarify the design components of GCTMs, and explain how each component affects downstream task performance (Section 4.1). In particular, flexible choice of couplings enable GCTM training in both unsupervised and supervised settings, allowing us to accelerate zero-shot and supervised image manipulation algorithms.
- **Empirical verification.** We demonstrate the potential of GCTMs on unconditional generation, image-to-image translation, image restoration, image editing, and latent manipulation. We show that GCTMs achieve competitive performance even with NFE = 1.

2 RELATED WORK

Diffusion model distillation. Despite the success of diffusion models (DMs) in generation tasks, DMs require large number of function evaluations (NFEs). As a way to improve the inference speed, the distillation method is proposed to predict the previously trained teacher DM’s output, *e.g.*, score function. Progressive distillation (PD) (Salimans & Ho, 2022) progressively reduces the NFEs by training the student model to learn predictions corresponding to two-steps of the teacher model’s deterministic sampling path. Consistency models (CMs) (Song et al., 2023) perform distillation by reducing the self-consistency function over the generative ODE. The above methodologies only consider the output of the ODE path. In contrast, consistency trajectory model (CTM) (Kim et al., 2024b) simultaneously learns the integral and infinitesimal changes of the PFODE trajectory. Our paper extends CTM to learn the PFODE trajectory between two arbitrary distributions.

Zero-shot image restoration via diffusion. Image restoration such as super-resolution, deblurring, and inpainting can be formulated as inverse problems, which obtain true signals from given observations. With the advancements in DMs serving as powerful priors, diffusion based inverse solvers have been explored actively. As a pioneering work, DDRM (Kawar et al., 2022) performs denoising steps on the spectral space of a linear corrupting matrix. DPS (Chung et al., 2022) and Π GDM (Song et al., 2022) propose posterior sampling by estimating the likelihood distribution through Jensen’s approximation and Gaussian assumption, respectively. While diffusion-based inverse solvers facilitate zero-shot image restoration, they often necessitate prolonged sampling times.

Image translation via diffusion. Conditional GAN-based Pix2Pix (Isola et al., 2017) specifies the task of translating one image into another image as image-to-image translation. SDEdit (Meng et al., 2022) avoids mode collapse and learning instabilities with GANs by utilizing DMs to translate edited images along SDEs. Palette (Saharia et al., 2022) proposed conditional DMs for image-to-image translation tasks. To address the Gaussian prior constraint with DMs, Schrödinger bridge (SB) or direct diffusion bridge (DDB) methods have been proposed to learn SDEs between arbitrary two distributions (Liu et al., 2023; Kim et al., 2024a; Delbracio & Milanfar, 2023b; Chung et al., 2023). However, models that follow SDEs often require large NFEs. In contrast, our model learns ODE paths between two arbitrary distributions and demonstrates competitive results with NFE = 1.

3 BACKGROUND

3.1 DIFFUSION MODELS

Diffusion models learn to reverse the process of corrupting data into Gaussian noise. Formally, the corruption process can be described by a forward SDE

$$d\mathbf{x}_t = \sqrt{2t} d\mathbf{w}_t \quad (1)$$

defined on the time interval $t \in (0, T)$. Given \mathbf{x}_0 distributed according to a data distribution $p(\mathbf{x}_0)$, (1) sends \mathbf{x}_0 to Gaussian noise as t increases from 0 to T . The reverse of the corruption process can be described by the reverse SDE

$$d\mathbf{x}_t = -2t\nabla \log p(\mathbf{x}_t) dt + \sqrt{2t} d\bar{\mathbf{w}}_t \quad (2)$$

or its deterministic counterpart, the probability flow ODE (PFODE)

$$d\mathbf{x}_t = -t\nabla \log p(\mathbf{x}_t) dt = t^{-1}(\mathbf{x}_t - \mathbb{E}_{p(\mathbf{x}_0|\mathbf{x}_t)}[\mathbf{x}_0]) dt \quad (3)$$

where $p(\mathbf{x}_t)$ is the distribution of \mathbf{x}_t following (1), and $\bar{\mathbf{w}}_t$ is the standard Wiener process in reverse-time. Given a noise sample $\mathbf{x}_T \sim p(\mathbf{x}_T)$, \mathbf{x}_t following (2) or (3) is distributed according to $p(\mathbf{x}_t)$ as t decreases from T to 0. Thus, diffusion models are able to generate data from noise by approximating the scores $\nabla \log p(\mathbf{x}_t)$ via score matching, and then numerically integrating (2) or (3).

3.2 CONSISTENCY TRAJECTORY MODELS (CTMs)

CTMs learn to translate samples between arbitrary time points of PFODE trajectories, *i.e.*, the goal of CTMs is to learn the integral of the PFODE

$$G(\mathbf{x}_t, t, s) := \mathbf{x}_t + \int_t^s u^{-1}(\mathbf{x}_u - \mathbb{E}_{p(\mathbf{x}_0|\mathbf{x}_u)}[\mathbf{x}_0]) du \quad (4)$$

for $s \leq t$, where the terminal distribution $p(\mathbf{x}_T)$ is assumed to be Gaussian. The parametrization

$$G(\mathbf{x}_t, t, s) = \frac{s}{t}\mathbf{x}_t + \left(1 - \frac{s}{t}\right)g(\mathbf{x}_t, t, s) \quad (5)$$

where

$$g(\mathbf{x}_t, t, s) = \mathbf{x}_t + \frac{t}{t-s} \int_t^s u^{-1}(\mathbf{x}_u - \mathbb{E}_{p(\mathbf{x}_0|\mathbf{x}_u)}[\mathbf{x}_0]) du \quad (6)$$

enables both traversal along the PFODE as well as score inference, since

$$\lim_{s \rightarrow t} g(\mathbf{x}_t, t, s) = \mathbb{E}_{p(\mathbf{x}_0|\mathbf{x}_t)}[\mathbf{x}_0] \quad (7)$$

so we may define $g(\mathbf{x}_t, t, t) := \mathbb{E}_{p(\mathbf{x}_0|\mathbf{x}_t)}[\mathbf{x}_0]$.

Given a pre-trained DM, CTMs approximate g with a neural net g_θ by simultaneously minimizing a distillation loss and a denoising score matching (DSM) loss. The distillation loss is

$$\mathcal{L}_{\text{CTM}}(\theta) := \mathbb{E}_{0 \leq s \leq u < t \leq T} \mathbb{E}_{p(\mathbf{x}_t)} [d(G_\theta(\mathbf{x}_t, t, s), G_{\text{sg}(\theta)}(\mathbf{x}_{t \rightarrow u}, u, s))] \quad (8)$$

where G_θ is (5) with g_θ in place of g , $d(\cdot, \cdot)$ is a measure of similarity between inputs, sg is the stop-gradient operation, and $\mathbf{x}_{t \rightarrow u}$ is defined to be the integral of PFODE from time t to u starting from \mathbf{x}_t using score estimates from the pre-trained diffusion model. Minimization of (8) causes G_θ to adhere to PFODE trajectories generated by the pre-trained diffusion model. The DSM loss is

$$\mathcal{L}_{\text{DSM}}(\theta) := \mathbb{E}_{0 \leq \hat{t} \leq T} \mathbb{E}_{p(\mathbf{x}_0)p(\mathbf{x}_1)} \mathbb{E}_{p(\mathbf{x}_{\hat{t}}|\mathbf{x}_0, \mathbf{x}_T)} [\|\mathbf{x}_0 - g_\theta(\mathbf{x}_{\hat{t}}, \hat{t}, \hat{t})\|_2^2] \quad (9)$$

where $p(\mathbf{x}_t|\mathbf{x}_0, \mathbf{x}_T) = \delta_{\mathbf{x}_0 + t\mathbf{x}_T}(\mathbf{x}_t)$, and minimization of (9) causes g_θ to satisfy (7). This loss acts as a regularization which improves score accuracy, and is crucial for sampling with large NFES. Thus, the final objective is

$$\mathcal{L}_{\text{CTM}}(\theta) + \lambda_{\text{DSM}} \mathcal{L}_{\text{DSM}}(\theta), \quad (10)$$

and it is possible to further improve sample quality by adding a GAN loss.

3.3 FLOW MATCHING (FM)

Flow Matching is another technique for learning PFODEs between two distributions $q(\mathbf{x}_0)$ and $q(\mathbf{x}_1)$. Specifically, let $q(\mathbf{x}_0, \mathbf{x}_1)$ be a joint distribution of \mathbf{x}_0 and \mathbf{x}_1 . Define

$$q(\mathbf{x}_t|\mathbf{x}_0, \mathbf{x}_1) := \delta_{(1-t)\mathbf{x}_0 + t\mathbf{x}_1}(\mathbf{x}_t), \quad q(\mathbf{x}_t) := \mathbb{E}_{q(\mathbf{x}_0, \mathbf{x}_1)} [q(\mathbf{x}_t|\mathbf{x}_0, \mathbf{x}_1)] \quad (11)$$

where $t \in (0, 1)$ and $\delta_{\mathbf{y}}(\cdot)$ is a Dirac delta at \mathbf{y} . Then the ODE given by

$$d\mathbf{x}_t = \mathbb{E}_{q(\mathbf{x}_0, \mathbf{x}_1|\mathbf{x}_t)} [\mathbf{x}_1 - \mathbf{x}_0] dt \quad (12)$$

generates the probability path $q(\mathbf{x}_t)$, i.e., with terminal condition $\mathbf{x}_1 \sim q(\mathbf{x}_1)$, \mathbf{x}_t following (12) is distributed according to $q(\mathbf{x}_t)$. Analogous to denoising score matching, the velocity term in (12) can be approximated by a neural network \mathbf{v}_ϕ which solves a regression problem

$$\min_{\phi} \mathbb{E}_{q(\mathbf{x}_0, \mathbf{x}_1, \mathbf{x}_t)} [\|(\mathbf{x}_1 - \mathbf{x}_0) - \mathbf{v}_\phi(\mathbf{x}_t, t)\|_2^2]. \quad (13)$$

Unlike diffusion whose terminal distribution $p(\mathbf{x}_T)$ is Gaussian, $q(\mathbf{x}_1)$ can be arbitrary. Also, we remark that the theory presented here is only a particular instance of FM called conditional FM.

4 GENERALIZED CONSISTENCY TRAJECTORY MODELS (GCTMs)

We now present GCTMs, which generalize CTMs to enable translation between arbitrary distributions. We begin with a crucial theorem which proves we can parametrize the solution to the FM ODE (12) in a form analogous to CTMs. The proof is deferred to Appendix C.1.

Theorem 1. *The ODE (12) is equivalent to*

$$d\mathbf{x}_t = t^{-1}(\mathbf{x}_t - \mathbb{E}_{q(\mathbf{x}_0|\mathbf{x}_t)}[\mathbf{x}_0]) dt \quad (14)$$

defined on $t \in (0, 1)$. Hence, we can express the solution to (12) as

$$G(\mathbf{x}_t, t, s) = \frac{s}{t} \mathbf{x}_t + \left(1 - \frac{s}{t}\right) g(\mathbf{x}_t, t, s) \quad (15)$$

$$\text{where } g(\mathbf{x}_t, t, s) = \mathbf{x}_t + \frac{t}{t-s} \int_t^s u^{-1} (\mathbf{x}_u - \mathbb{E}_{q(\mathbf{x}_0|\mathbf{x}_u)}[\mathbf{x}_0]) du. \quad (16)$$

There are two differences between (5) and (15). First, the time variables t and s now lie in the unit interval $(0, 1)$ instead of $(0, T)$, and second, $p(\mathbf{x}_0|\mathbf{x}_u)$ is replaced with $q(\mathbf{x}_0|\mathbf{x}_u)$. The second difference is what enables translation between arbitrary distributions, as $q(\mathbf{x}_0|\mathbf{x}_u)$ recovers clean images \mathbf{x}_0 given images \mathbf{x}_u perturbed by arbitrary type of vectors (e.g., Gaussian noise, images, etc.), while $p(\mathbf{x}_0|\mathbf{x}_u)$ recovers clean images \mathbf{x}_0 only for Gaussian-perturbed samples \mathbf{x}_u . We call a neural network g_θ which approximates (16) a GCTM, and we can train such a network by optimizing the FM counterparts of \mathcal{L}_{CTM} and \mathcal{L}_{DSM} :

$$\mathcal{L}_{\text{GCTM}}(\theta) := \mathbb{E}_{0 \leq s \leq u < t \leq 1} \mathbb{E}_{q(\mathbf{x}_t)} [d(G_\theta(\mathbf{x}_t, t, s), G_{\text{sg}(\theta)}(\mathbf{x}_{t \rightarrow u}, u, s))] \quad (17)$$

where G_θ is (15) with g replaced by g_θ , and

$$\mathcal{L}_{\text{FM}}(\theta) := \mathbb{E}_{0 \leq \hat{t} \leq 1} \mathbb{E}_{q(\mathbf{x}_0, \mathbf{x}_1)} \mathbb{E}_{q(\mathbf{x}_i | \mathbf{x}_0, \mathbf{x}_1)} [\|\mathbf{x}_0 - g_\theta(\mathbf{x}_i, \hat{t}, \hat{t})\|_2^2]. \quad (18)$$

The next theorem shows that the PFODE (3) learned by CTMs is a special case of the ODE (14) learned by GCTMs, so GCTMs indeed generalize CTMs. The proof is deferred to Appendix C.2.

Theorem 2. Consider the choice of $q(\mathbf{x}_0, \mathbf{x}_1) = p(\mathbf{x}_0) \cdot \mathcal{N}(\mathbf{x}_1 | \mathbf{0}, \mathbf{I})$. Let

$$t' := t/(1+t), \quad \bar{\mathbf{x}}_{t'} := \mathbf{x}_t/(1+t) \quad (19)$$

where $t \in (0, \infty)$ and \mathbf{x}_t follows the PFODE (3). Then

$$\mathbb{E}_{p(\mathbf{x}_0 | \mathbf{x}_t)}[\mathbf{x}_0] = \mathbb{E}_{q(\mathbf{x}_0 | \bar{\mathbf{x}}_{t'})}[\mathbf{x}_0] \quad (20)$$

and $\bar{\mathbf{x}}_{t'}$ follows the ODE

$$d\bar{\mathbf{x}}_{t'} = t'^{-1}(\bar{\mathbf{x}}_{t'} - \mathbb{E}_{q(\mathbf{x}_0 | \bar{\mathbf{x}}_{t'})}[\mathbf{x}_0]) dt' \quad (21)$$

on $t' \in (0, 1)$. Furthermore, let $G_{\text{CTM}}, g_{\text{CTM}}$ denote CTM solutions and let $G_{\text{GCTM}}, g_{\text{GCTM}}$ denote GCTM solutions. Then with $s' = s/(1+s)$,

$$\begin{cases} G_{\text{CTM}}(\mathbf{x}_t, t, s) = G_{\text{GCTM}}(\bar{\mathbf{x}}_{t'}, t', s') \cdot (1+s) \\ g_{\text{CTM}}(\mathbf{x}_t, t, t) = g_{\text{GCTM}}(\bar{\mathbf{x}}_{t'}, t', t') \end{cases} \quad (22)$$

In short, (20) shows the equivalence of scores, and (21) shows the equivalence of ODEs. Thus, given g_θ trained with \mathcal{L}_{FM} and $\mathcal{L}_{\text{GCTM}}$ with the setting of Thm. 1, we are able to evaluate diffusion scores and simulate diffusion PFODE trajectories with a simple change of variables (19), as shown in (22).

Given GCTM's capability to replicate CTM, we will now outline the key components of GCTM that enable its significant extension for various downstream tasks. This flexibility offers a notable advantage of GCTM over CTM.

4.1 THE DESIGN SPACE OF GCTMS

Coupling $q(\mathbf{x}_0, \mathbf{x}_1)$. In contrast to diffusion which only uses the trivial coupling $q(\mathbf{x}_0, \mathbf{x}_1) = q(\mathbf{x}_0)q(\mathbf{x}_1)$ in $\mathcal{L}_{\text{DSM}}(\theta)$, FM allows us to use arbitrary joint distributions of $q(\mathbf{x}_0)$ and $q(\mathbf{x}_1)$ in $\mathcal{L}_{\text{FM}}(\theta)$. Intuitively, $q(\mathbf{x}_0, \mathbf{x}_1)$ encodes our inductive bias for what kind of pairs $(\mathbf{x}_0, \mathbf{x}_1)$ we wish the model to learn, since FM ODE is distributed $q(\mathbf{x}_t)$ at each time t , and $q(\mathbf{x}_t)$ is the distribution of $(1-t)\mathbf{x}_0 + t\mathbf{x}_1$ for $(\mathbf{x}_0, \mathbf{x}_1) \sim q(\mathbf{x}_0, \mathbf{x}_1)$. Here, we list three valid couplings of GCTM as examples (see Alg. 1 for code). In contrast, CTM only use a special case of independence coupling.

- *Independent coupling:*

$$q(\mathbf{x}_0, \mathbf{x}_1) = q(\mathbf{x}_0)q(\mathbf{x}_1) \quad (23)$$

This coupling reflects no prior assumption about the relation between \mathbf{x}_0 and \mathbf{x}_1 . As shown earlier, diffusion models use this type of coupling.

- *(Entropy-regularized) Optimal transport coupling:*

$$q = \arg \min_{\tilde{q}} \mathbb{E}_{\tilde{q}(\mathbf{x}_0, \mathbf{x}_1)} [\|\mathbf{x}_0 - \mathbf{x}_1\|_2^2] - \tau H(\tilde{q}) \quad (24)$$

where $\arg \min$ is over all joint distributions \tilde{q} of $q(\mathbf{x}_0)$ and $q(\mathbf{x}_1)$, H denotes entropy, and τ is the regularization coefficient. This coupling reflects the inductive bias that \mathbf{x}_0 and \mathbf{x}_1 must be close together under the Euclidean distance. In practice, we use the Sinkhorn-Knopp (SK) algorithm (Cuturi, 2013) to sample OT pairs. A pseudo-code for SK is given as Alg. 3 in Appendix B.

- *Supervised coupling:*

$$q(\mathbf{x}_0, \mathbf{x}_1) = \int q(\mathbf{x}_0)q(\mathbf{H}|\mathbf{x}_0)\delta_{\mathbf{H}\mathbf{x}_0}(\mathbf{x}_1) d\mathbf{H} \quad (25)$$

where $\mathbf{H} \sim q(\mathbf{H}|\mathbf{x}_0)$ is a random operator, possibly dependent on \mathbf{x}_0 , which maps ground-truth data \mathbf{x}_0 to observations \mathbf{x}_1 , i.e., $\mathbf{x}_1 = \mathbf{H}\mathbf{x}_0$. For instance, in the context of learning an inpainting model, \mathbf{H} is could be a random masking operator. For a fixed \mathbf{H} , $q(\mathbf{H}|\mathbf{x}_0)$ reduces to a Dirac delta. With this coupling, the ODE (14) tends to map observed samples \mathbf{x}_1 to ground-truth data \mathbf{x}_0 as $t \rightarrow 0$.

Algorithm 1 $q(x_0, x_1)$ Sampling

```

1: Assume  $m = 1, \dots, M$ , Batch size  $M$ 
2: if Coupling is Independent then
3:    $\{x_0^m\}_m \sim q(x_0), \{x_1^m\}_m \sim q(x_1)$ 
4:   Return  $\{(x_0^m, x_1^m)\}_m$ 
5: else if Coupling is OT then
6:    $\{x_0^m\}_m \sim q(x_0), \{x_1^m\}_m \sim q(x_1)$ 
7:   Return SK( $\{x_0^m\}_m, \{x_1^m\}_m, \tau$ )
8: else if Coupling is Supervised then
9:    $\{x_0^m\}_m \sim q(x_0), H^m \sim q(H|x_0^m)$ 
10:  Return  $\{(x_0^m, H^m x_0^m)\}_m$ 
11: end if

```

Algorithm 2 GCTM Training

```

1: while training do
2:   Sample times  $\{\hat{t}^m\}_m, \{(t^m, s^m, u^m)\}_m$ 
3:   With Alg. 1,  $\{(x_0^m, x_1^m)\}_m \sim q(x_0, x_1)$ 
4:    $x_{\hat{t}^m}^m \leftarrow (1 - \hat{t}^m)x_0^m + \hat{t}^m x_1^m$ 
5:    $x_{t^m}^m \leftarrow (1 - t^m)x_0^m + t^m x_1^m$ 
6:    $\mathcal{L}_{\text{FM}}(\theta) = \frac{1}{M} \sum_m \|x_0^m - g_\theta(x_{\hat{t}^m}^m, \hat{t}^m, \hat{s}^m)\|_2^2$ 
7:    $\tilde{x}_{s^m}^m \leftarrow G_{\text{sg}(\theta)}(x_{t^m}^m \rightarrow u^m, u^m, s^m)$ 
8:    $\mathcal{L}_{\text{GCTM}}(\theta) = \frac{1}{M} \sum_{m=1}^M d(G_\theta(x_{t^m}^m, t^m, s^m), \tilde{x}_{s^m}^m)$ 
9:   Minimize  $\mathcal{L}_{\text{GCTM}}(\theta) + \lambda_{\text{FM}} \mathcal{L}_{\text{FM}}(\theta)$ 
10: end while

```

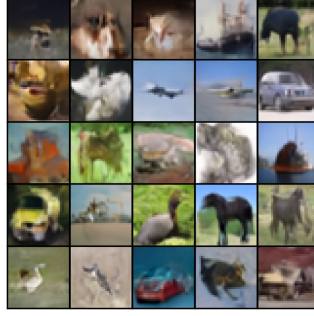
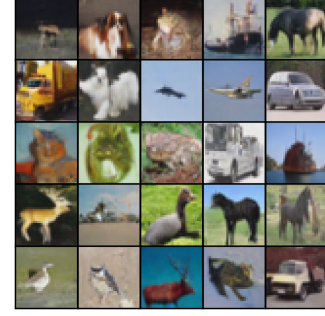
(a) Indep. $N = 4$, FID = 24.7(b) OT $N = 4$, FID = 18.2(c) OT $N = 32$, FID = 5.32

Figure 2: CIFAR10 unconditional samples with NFE = 1.

Gaussian perturbation. The cardinality of the support of $q(x_1)$ must be larger than or equal to the cardinality of the support of $q(x_0)$ for there to be a well-defined ODE from $q(x_1)$ to $q(x_0)$. This is because the ODE trajectory given an initial condition is unique, so a single sample $x_1 \sim q(x_1)$ cannot be transported to multiple points in the support of $q(x_0)$. A simple way to address this problem is to add small Gaussian noise to $q(x_1)$ samples such that $q(x_1)$ is supported everywhere.

We emphasize that Gaussian perturbation allows GCTMs to achieve one-to-many generation when we use the supervised coupling. Concretely, consider the scenario where there are multiple labels $x_0 \sim q(x_0|x_1)$ which correspond to an observed x_1 . Then, the perturbation ϵ added to x_1 acts as a source of randomness, allowing the GCTM network to map $x_1 + \epsilon$ to distinct labels x_0 for distinct ϵ . This stands in contrast to simply regressing the neural network output of x_1 to corresponding labels $x_0 \sim q(x_0|x_1)$ with ℓ_2 loss, as this will cause the network to map x_1 to the blurry posterior mean $\mathbb{E}_{q(x_0|x_1)}[x_0]$ instead of a sharp image x_0 . Indeed, in Section 5.2, we observe blurry outputs if we use regression instead of GCTMs.

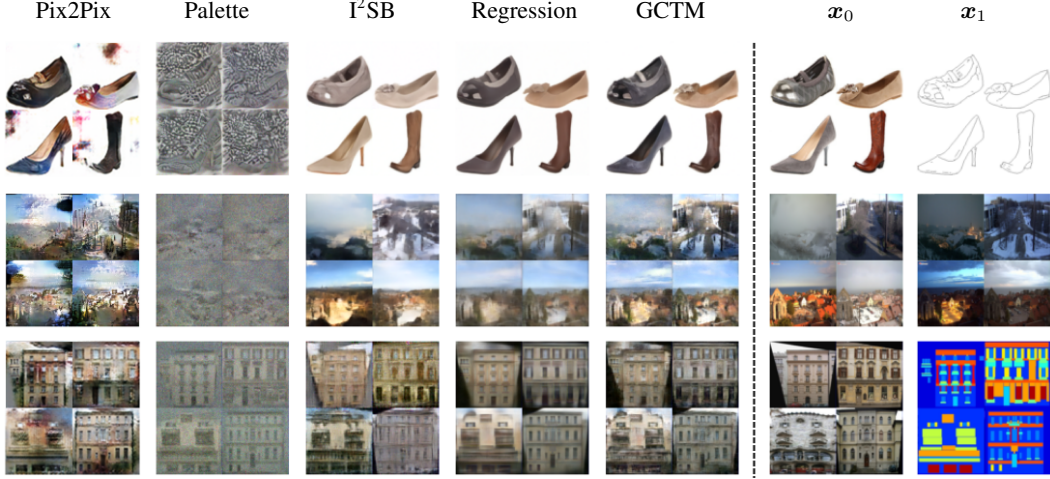
5 EXPERIMENTS

We now explore the possibilities of GCTMs on unconditional generation, image-to-image translation, image restoration, image editing, and latent manipulation. In particular, GCTM admits NFE = 1 sampling via $x_t \mapsto G_\theta(x_t, t, 0)$. Due to the similarities between CTMs and GCTMs as detailed in Thm. 1, GCTMs can be trained using CTM training methods. In fact, we run Alg. 2 with the method in Section 5.2 of (Kim et al., 2024b) to train all GCTMs without pre-trained teacher models. A complete description of training settings are deferred to Appendix A.

5.1 FAST UNCONDITIONAL GENERATION

In the scenario where we do not have access to data pairs, we must resort to either the independent coupling or the OT coupling. Here, we show that the optimal transport coupling can significantly accelerate the convergence speed of GCTMs during training, especially when we use a smaller number of timesteps N .

Method	NFE	Time (ms)	Edges→Shoes			Night→Day			Facades		
			FID ↓	IS ↑	LPIPS ↓	FID ↓	IS ↑	LPIPS ↓	FID ↓	IS ↑	LPIPS ↓
Regression	1	87	54.3	3.41	0.100	189.2	1.85	0.373	121.8	3.28	0.274
Pix2Pix (Isola et al., 2017)	1	33	77.0	3.17	0.208	158.0	1.68	0.418	134.1	2.74	0.288
Palette (Saharia et al., 2022)	5	166	334.1	1.90	0.861	350.2	1.16	0.707	259.3	2.47	0.394
I ² SB (Liu et al., 2023)	5	284	<u>53.9</u>	3.23	0.154	145.8	1.79	0.376	135.2	2.51	0.269
GCTM	1	87	40.3	3.54	0.097	<u>148.8</u>	2.00	0.317	111.3	<u>2.99</u>	0.230

Table 2: Quantitative evaluation of I2I translation. Best is in **bold**, second best is underlined.Figure 4: Qualitative evaluation of image-to-image translation on Edges→Shoes (top), Night→Day (middle) and Facades (bottom). NFE = 5 for I²SB and Palette.

Using small N may be of interest when we wish to trade-off training speed for performance, since per-iteration training cost of GCTMs increases linearly with N . For instance, when $t = 1$ and $u = s = 0$ in the GCTM loss (17), we need to integrate along the entire time interval $(0, 1)$, which requires N steps of ODE integration.

In Figure 3, we observe up to $\times 2.5$ acceleration in terms of training iterations when we use OT coupling instead of independent coupling. Indeed, in Figure 2, OT coupling samples are visually sharper than independent coupling samples. We postulate this is because (1) OT coupling leads to straighter ODE trajectories, so we can accurately integrate ODEs with smaller N , and (2) lower variance from OT pairs leads to smaller variance in loss gradients, as discussed in (Pooladian et al., 2023).

In Table 1, we compare the Fréchet Inception Distance (FID) (Heusel et al., 2017) of GCTM and relevant base-lines on CIFAR10 with NFE = 1. In the setting where we do not use a pre-trained teacher diffusion model, GCTM with OT coupling outperforms all methods with the exception of iCM (Song & Dhariwal, 2024), which is an improved variant of CM. Moreover, GCTM is on par with CTM trained with a teacher. We speculate that further fine-tuning of hyper-parameters could push the performance of GCTMs to match that of iCMs, and we leave this for future work.

5.2 FAST IMAGE-TO-IMAGE TRANSLATION

Unlike previous distillation methods such as CM or CTM, GCTM can learn ODEs between arbitrary distributions, enabling image-to-image translation. To numerically validate this theoretical improvement, we train GCTMs on three translation tasks Edges→Shoes, Night→Day, and Facades (Isola et al., 2017), scaled to 64×64 , with the supervised coupling. We consider three baseline methods:

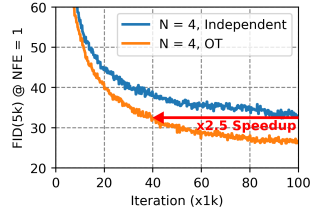


Figure 3: Training acceleration.

Method	Teacher	FID ↓
CTM	✓	5.28
	✗	9.00
CM	✓	3.55
	✗	8.70
iCM	✗	2.51
GCTM (OT)	✗	5.32

Table 1: FID at NFE = 1.

	Method	NFE	Time (ms)	SR2 - Bicubic			Deblur - Gaussian			Inpaint - Center		
				PSNR \uparrow	SSIM \uparrow	LPIPS \downarrow	PSNR \uparrow	SSIM \uparrow	LPIPS \downarrow	PSNR \uparrow	SSIM \uparrow	LPIPS \downarrow
<i>0-Shot</i>	DPS	32	1079	31.19	0.935	<u>0.015</u>	27.88	0.878	0.041	24.69	0.876	0.042
	CM	32	1074	30.80	0.930	0.010	27.85	0.871	0.027	23.02	0.857	0.050
	GCTM	32	1382	31.61	0.939	<u>0.015</u>	28.19	0.885	<u>0.037</u>	<u>24.47</u>	0.876	0.042
<i>Superv.</i>	Regression	1	87	33.46	0.964	0.015	31.19	0.942	0.015	28.76	0.922	0.028
	Palette	5	166	17.88	0.556	0.234	17.81	0.571	0.234	16.12	0.489	0.357
	I ² SB	5	284	26.74	0.869	0.033	26.20	0.853	0.038	26.01	0.874	0.038
	GCTM	1	87	<u>32.37</u>	<u>0.954</u>	0.009	<u>30.56</u>	<u>0.935</u>	0.009	<u>27.37</u>	<u>0.896</u>	0.027

Table 3: Quantitative evaluation of image restoration on FFHQ.

ℓ_2 -regression, Pix2Pix (Isola et al., 2017), Palette (Saharia et al., 2022) and I²SB (Liu et al., 2023). To evaluate translation performance, we use FID and Inception Score (IS) (Barratt & Sharma, 2018) to rate translation quality and LPIPS (Zhang et al., 2018) to assess faithfulness to input. We control NFEs such that all methods have similar inference times, and we calculate all metrics on validation samples.

In Table 2, we see GCTM shows strong performance on all tasks. In particular, GCTM is good at preserving input structure, as supported by low LPIPS values. SDE-based methods I²SB and Palette show poor performance at low NFEs, even when trained with pairs. Qualitative results in Figure 4 are in line with the metrics. Baselines produce blurry or nonsensical samples, while GCTM produces sharp and realistic images that are faithful to the input.

5.3 FAST IMAGE RESTORATION

We consider two settings on the FFHQ 64×64 dataset, where we either know or do not know the corruption operator. In the former case, we train an unconditional GCTM with the independent coupling, with which we implement three zero-shot image restoration algorithms: DPS, CM-based image restoration, and the guided generation algorithm illustrated in Figure 1, where the loss is given as inconsistency between observations (see Append. B.2 for pseudo-codes and a detailed discussion of the differences). In the latter case, we train a GCTM with the supervised coupling and ℓ_2 -regression, I²SB and Palette for comparison. Notably, GCTM is the only model applicable to both situations, thanks to the flexible choice of couplings. We again control NFEs such that all methods have similar inference speed.



Figure 5: Reg. vs. GCTM.

Table 3 presents the numerical results in both settings. In the zero-shot setting, we see GCTM outperforming both DPS and CM. In particular, CM is slightly worse than DPS. Sample quality degradation due to error accumulation for CMs at large NFEs have already been observed in unconditional generation (e.g., see Fig. 9 in (Kim et al., 2024b)), and we speculate a similar problem occurs for CMs in image restoration as well. On the other hand, GCTMs avoid this problem, as they are able to traverse to a smaller time using the ODE velocity approximated via g_θ . In the supervised setting, we see regression attains the best PSNR and SSIM. This is a natural consequence of perception-distortion trade-off. Specifically, regression minimizes the MSE loss, so it leads to best distortion metrics (Delbracio & Milanfar, 2023a) while producing blurry results. GCTM, which provides best results if we exclude regression on distortion metrics (PSNR and SSIM) and best results on perception metrics (LPIPS), strikes the best balance between perception and distortion. For instance, in Fig. 5 inpainting results, regression sample lacks detail (e.g., wrinkles) while GCTM sample is sharp. We show more samples in Appendix E. In particular, in Table 5, we demonstrate image restoration task of GCTM on ImageNet with higher resolution (256×256 resolution) to demonstrate its scalability.

5.4 FAST IMAGE EDITING

In this section, we demonstrate that GCTM can perform realistic and faithful image editing without any special purpose training. Figure 6 shows image editing with an Edges→Shoes model and an unconditional FFHQ model. On Edges→Shoes, to edit an image, a user creates an edited input,

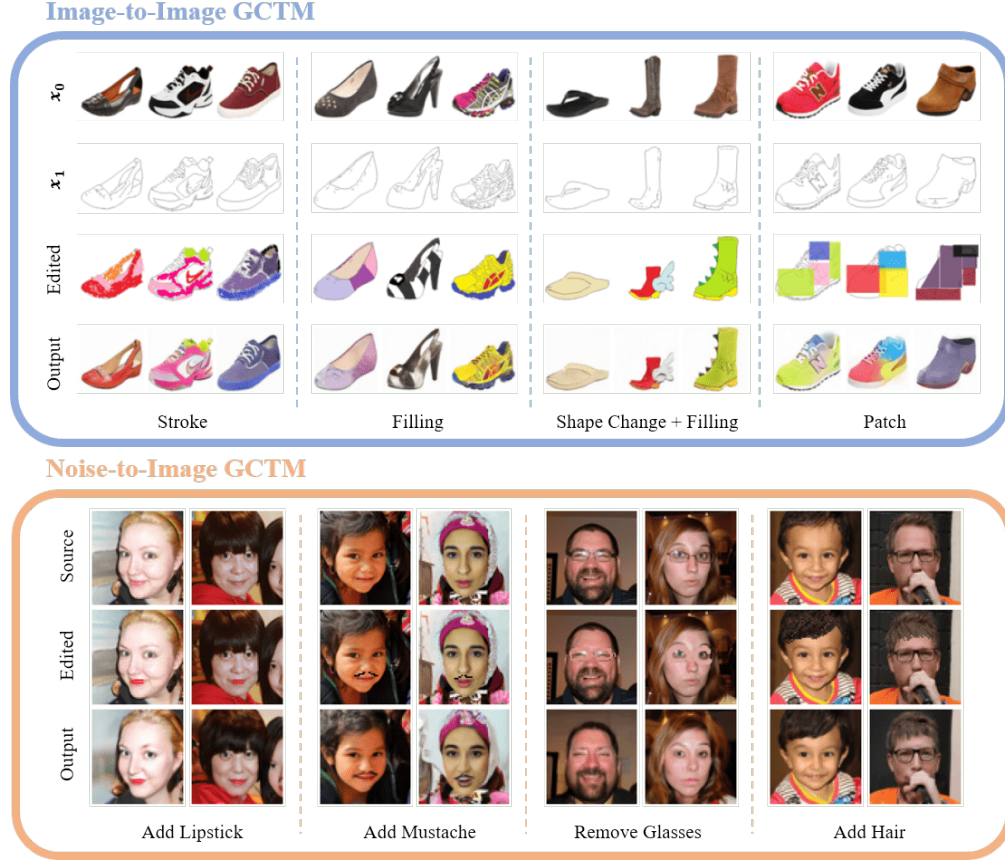


Figure 6: Image editing with GCTM, NFE = 1.

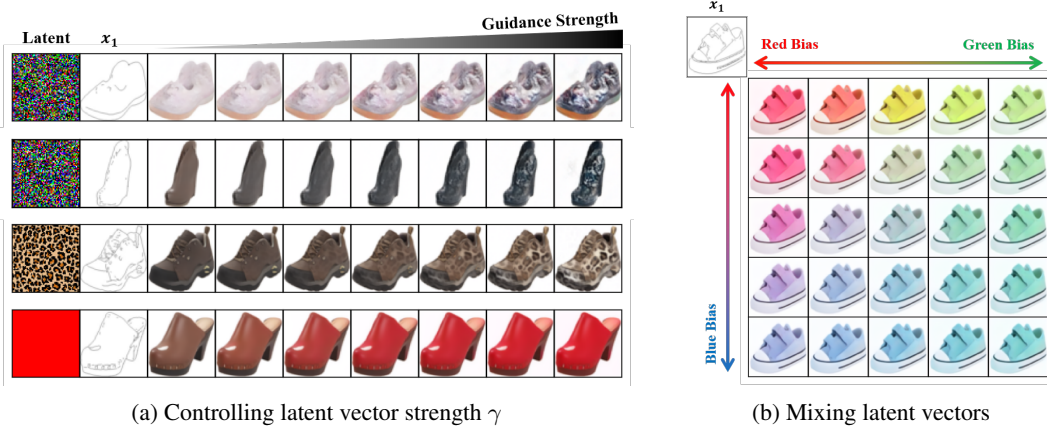


Figure 7: Latent manipulation with image-to-image GCTM, NFE = 1.

which is an edge image painted to have a desired color and / or modified to have a desired outline. We then interpolate the edited input and the original edge image to a certain time point $t = s$ and send it to time $t = 0$ with GCTM to produce the output. On FFHQ, analogous to SDEdit (Meng et al., 2022), we interpolate an edited image with Gaussian noise and send it to time $t = 0$ with GCTM to generate the output. In contrast to previous image editing models such as SDEdit, GCTM requires only a single step to edit an image. Moreover, we observe that GCTM faithfully preserves source image structure while making the desired changes to the image.

5.5 FAST LATENT MANIPULATION

In this section, we demonstrate that GCTMs have a highly controllable latent space. Since there are plenty of works on latent manipulation with unconditional diffusion models, we focus on latent manipulation with GCTMs trained for image-to-image translation. For an image-to-image translation GCTM trained with Gaussian perturbation in Section 4.1, we assert that the perturbation added to x_1 can be manipulated to produce desired outputs x_0 . In other words, the perturbation acts as a “latent vector” which controls the factors of variation in x_0 . To test this hypothesis, in Figure 7, we display outputs $G_\theta(x_1 + \gamma\epsilon, 1, 0)$ for particular choices of ϵ . In the left panel, we observe generated outputs increasingly adhere to the texture of latent ϵ as we increase guidance strength γ . Interestingly, GCTM generalizes well to latent vectors unseen during training, such as leopard spots or the color red. In the right panel, we explore the effect of linearly combining red, green, and blue latent vectors. We see that the desired color change is reflected faithfully in the outputs. These observations validate our hypothesis that image-to-image GCTMs have an interpretable latent space.

5.6 ABLATION STUDY

We now perform an ablation study on the design choices of Section 4.1. We have already illustrated the power of using appropriate couplings in previous sections, so we explore the importance of σ_{\max} . A robust choice for σ_{\max} for unconditional generation is well-known to be $\sigma_{\max} = 80$ (Karras et al., 2022; Kim et al., 2024b), and we found using this choice to perform sufficiently well for GCTMs when learning to translate noise to data with independent or OT couplings. So, we restrict our attention to image-to-image translation.

In Figure 8, we display the learning curves on Edges→Shoes for GCTMs trained without and with Gaussian perturbation, and $\sigma_{\max} \in \{80, 500\}$. We observe that GCTM trained without perturbation and $\sigma_{\max} = 80$ exhibits unstable dynamics, and is unable to minimize the FID below 30. On other hand, GCTM trained with perturbation and $\sigma_{\max} = 80$ surpasses the model trained without perturbation. This demonstrates Gaussian perturbation is indeed crucial for one-to-many generation, as noted in the last paragraph of Section 4.1. Finally, GCTM with both perturbation and $\sigma_{\max} = 500$ minimizes FID the fastest. This shows high-curvature regions for image-to-image ODEs lie near x_1 , so we need to use a large σ_{\max} which places more discretization points near $t = 1$.

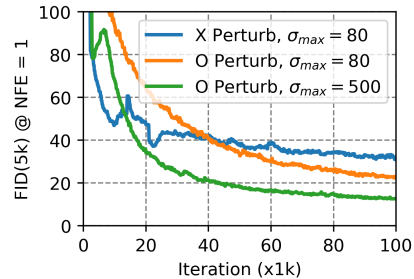


Figure 8: Ablation study of GCTM.

6 CONCLUSION

Our work marks a significant advancement in the realm of ODE-based generative models, particularly on the transformative capabilities of Consistency Trajectory Models (CTMs). While the iterative nature of diffusion has proven to be a powerful foundation for high-quality image synthesis and nuanced control, the computational demands associated with numerous neural function evaluations (NFEs) per sample have posed challenges for practical implementation. Our proposal of Generalized CTMs (GCTMs) extends the reach of CTMs by enabling one-step translation between arbitrary distributions, surpassing the limitations of traditional CTMs confined to Gaussian noise to data transformations. Through an insightful exploration of the design space, we elucidate the impact of various components on downstream task performance, providing a comprehensive understanding that contributes to a broadly applicable and stable training scheme. Empirical validation across diverse image manipulation tasks demonstrates the potency of GCTMs, showcasing their ability to accelerate and enhance diffusion-based algorithms. In summary, our work not only contributes to theoretical advancements but also delivers tangible benefits, showcasing GCTMs as a key element in unlocking the full potential of diffusion models for practical, real-world applications in image synthesis, translation, restoration, and editing.

REFERENCES

- Shane Barratt and Rishi Sharma. A note on the inception score. *arXiv preprint arXiv:1801.01973*, 2018.
- Hyungjin Chung, Jeongsol Kim, Michael T Mccann, Marc L Klasky, and Jong Chul Ye. Diffusion posterior sampling for general noisy inverse problems. *arXiv preprint arXiv:2209.14687*, 2022.
- Hyungjin Chung, Jeongsol Kim, and Jong Chul Ye. Direct diffusion bridge using data consistency for inverse problems. *arXiv preprint arXiv:2305.19809*, 2023.
- Marco Cuturi. Sinkhorn distances: Lightspeed computation of optimal transport. *NeurIPS*, 2013.
- Mauricio Delbracio and Peyman Milanfar. Inversion by direct iteration: An alternative to denoising diffusion for image restoration. *arXiv preprint arXiv:2303.11435*, 2023a.
- Mauricio Delbracio and Peyman Milanfar. Inversion by direct iteration: An alternative to denoising diffusion for image restoration. *arXiv preprint arXiv:2303.11435*, 2023b.
- Prafulla Dhariwal and Alexander Nichol. Diffusion models beat gans on image synthesis. *NeurIPS*, 34:8780–8794, 2021.
- Ian Goodfellow, Jean Pouget-Abadie, Mehdi Mirza, Bing Xu, David Warde-Farley, Sherjil Ozair, Aaron Courville, and Yoshua Bengio. Generative adversarial networks. *Communications of the ACM*, 63(11):139–144, 2020.
- Martin Heusel, Hubert Ramsauer, Thomas Unterthiner, Bernhard Nessler, and Sepp Hochreiter. Gans trained by a two time-scale update rule converge to a local nash equilibrium. *NeurIPS*, 30, 2017.
- Jonathan Ho and Tim Salimans. Classifier-free diffusion guidance. *arXiv preprint arXiv:2207.12598*, 2022.
- Jonathan Ho, Ajay Jain, and Pieter Abbeel. Denoising diffusion probabilistic models. *NeurIPS*, 33: 6840–6851, 2020.
- Phillip Isola, Jun-Yan Zhu, Tinghui Zhou, and Alexei A Efros. Image-to-image translation with conditional adversarial networks. In *CVPR*, 2017.
- Tero Karras, Miika Aittala, Timo Aila, and Samuli Laine. Elucidating the design space of diffusion-based generative models. *NeurIPS*, 2022.
- Bahjat Kavar, Michael Elad, Stefano Ermon, and Jiaming Song. Denoising diffusion restoration models. *Advances in Neural Information Processing Systems*, 35:23593–23606, 2022.
- Beomsu Kim, Gihyun Kwon, Kwanyoung Kim, and Jong Chul Ye. Unpaired image-to-image translation via neural Schrödinger bridge. *ICLR*, 2024a.
- Dongjun Kim, Chieh-Hsin Lai, Wei-Hsiang Liao, Naoki Murata, Yuhta Takida, Toshimitsu Uesaka, Yutong He, Yuki Mitsufuji, and Stefano Ermon. Consistency trajectory models: Learning probability flow ode trajectory of diffusion. *ICLR*, 2024b.
- Diederik P. Kingma and Jimmy Ba. Adam: A method for stochastic optimization. *ICLR*, 2015.
- Diederik P Kingma and Max Welling. Auto-encoding variational bayes. *arXiv preprint arXiv:1312.6114*, 2013.
- Bo Li, Kaitao Xue, Bin Liu, and Yu-Kun Lai. Bbim: Image-to-image translation with brownian bridge diffusion models. In *Proceedings of the IEEE/CVF conference on computer vision and pattern Recognition*, pp. 1952–1961, 2023.
- Yaron Lipman, Ricky T. Q. Chen, Heli Ben-Hamu, Maximilian Nickel, and Matthew Le. Flow matching for generative modeling. *ICLR*, 2023.
- Guan-Horng Liu, Arash Vahdat, De-An Huang, Evangelos A Theodorou, Weili Nie, and Anima Anandkumar. I²SB: Image-to-image Schrödinger bridge. *ICML*, 2023.

- Chenlin Meng, Yutong He, Yang Song, Jiaming Song, Jiajun Wu, Jun-Yan Zhu, and Stefano Ermon. SDEdit: Guided image synthesis and editing with stochastic differential equations. *ICLR*, 2022.
- Aram-Alexandre Pooladian, Heli Ben-Hamu, Carles Domingo-Enrich, Brandon Amos, Yaron Lipman, and Ricky T. Q. Chen. Multisample flow matching: Straightening flows with minibatch couplings. *ICML*, 2023.
- Chitwan Saharia, William Chan, Huiwen Chang, Chris Lee, Jonathan Ho, Tim Salimans, David Fleet, and Mohammad Norouzi. Palette: Image-to-image diffusion models. In *SIGGRAPH*, 2022.
- Tim Salimans and Jonathan Ho. Progressive distillation for fast sampling of diffusion models. *ICLR*, 2022.
- Jiaming Song, Arash Vahdat, Morteza Mardani, and Jan Kautz. Pseudoinverse-guided diffusion models for inverse problems. In *International Conference on Learning Representations*, 2022.
- Yang Song and Prafulla Dhariwal. Improved techniques for training consistency models. *ICLR*, 2024.
- Yang Song, Jascha Sohl-Dickstein, Diederik P Kingma, Abhishek Kumar, Stefano Ermon, and Ben Poole. Score-based generative modeling through stochastic differential equations. *arXiv preprint arXiv:2011.13456*, 2020.
- Yang Song, Prafulla Dhariwal, Mark Chen, and Ilya Sutskever. Consistency models. *ICML*, 2023.
- Richard Zhang, Phillip Isola, Alexei A Efros, Eli Shechtman, and Oliver Wang. The unreasonable effectiveness of deep features as a perceptual metric. In *CVPR*, pp. 586–595, 2018.
- Min Zhao, Fan Bao, Chongxuan Li, and Jun Zhu. Egsde: Unpaired image-to-image translation via energy-guided stochastic differential equations. *Advances in Neural Information Processing Systems*, 35:3609–3623, 2022.

A FULL EXPERIMENT SETTINGS

A.1 TRAINING

In this section, we introduce training choices which provided reliable performance across all experiments in our paper.

Bootstrapping scores. In all our experiments, we train GCTMs without a pre-trained score model. So, analogous to CTMs, we use velocity estimates given by an exponential moving average θ_{EMA} of θ to solve ODEs. We use exponential moving average decay rate 0.999.

Time discretization. In practice, we discretize the unit interval into a finite number of timesteps $\{t_n\}_{n=0}^N$ where

$$t_0 = 0 < t_1 < \dots < t_N = 1 \quad (26)$$

and learn ODE trajectories integrated with respect to the discretization schedule. EDM (Karras et al., 2022), which has shown robust performance on a variety of generation tasks, solves the PFODE on the time interval $(\sigma_{\min}, \sigma_{\max})$ for $0 < \sigma_{\min} < \sigma_{\max}$ according to the discretization schedule

$$\sigma_n = (\sigma_{\min}^{1/\rho} + (n/N)(\sigma_{\max}^{1/\rho} - \sigma_{\min}^{1/\rho}))^\rho \quad (27)$$

for $n = 0, \dots, N$ and $\rho = 7$. Thus, using the change of time variable (19) derived in Theorem 1, we convert PFODE EDM schedule to FM ODE discretization

$$t_0 = 0, \quad t_n = \sigma_n / (1 + \sigma_n) \quad \text{for } n = 1, \dots, N-1, \quad t_N = 1. \quad (28)$$

In our experiments, we fix $\sigma_{\min} = 0.002$ and control σ_{\max} . We note that σ_{\max} controls the amount of emphasis on time near $t = 1$, i.e., larger σ_{\max} places more time discretization points near $t = 1$.

Number of discretization steps N . CTMs use fixed $N = 18$. In contrast, analogous to iCMs, we double N every 100k iterations, starting from $N = 4$.

Time \hat{t} distribution. For unconditional generation, we sample

$$\hat{t} = \sigma / (1 + \sigma), \quad \log \sigma \sim \mathcal{N}(-1.2, 1.2^2) \quad (29)$$

in accordance with EDM. For image-to-image translation, we sample

$$\hat{t} \sim \text{beta}(3, 1). \quad (30)$$

Network conditioning. We use the EDM conditioning, following CTMs.

Distance d . CTMs use d defined as

$$d(\mathbf{x}_t, \hat{\mathbf{x}}_t) = \text{LPIPS}(G_{\theta_{\text{EMA}}}(\mathbf{x}_t, t, 0), G_{\theta_{\text{EMA}}}(\hat{\mathbf{x}}_t, t, 0)) \quad (31)$$

which compares the perceptual distance of samples projected to time $t = 0$. In contrast, following iCMs, we use the pseudo-huber loss

$$d(\mathbf{x}_t, \hat{\mathbf{x}}_t) = \sqrt{\|\mathbf{x}_t - \hat{\mathbf{x}}_t\|_2^2 + c^2} - c \quad (32)$$

where $c = 0.00054\sqrt{d}$, where d is the dimension of \mathbf{x}_t .

Batch size. We use batch size 128 for 32×32 resolution images and batch size 64 for 64×64 resolution images.

Optimizer. We use the Adam optimizer (Kingma & Ba, 2015) with learning rate

$$\eta = 0.0002 / (128 / \text{batch_size}) \quad (33)$$

and default $(\beta_1, \beta_2) = (0.9, 0.999)$.

Coefficient for $\mathcal{L}_{\text{FM}}(\theta)$. We use $\lambda_{\text{FM}} = 0.1$ for all experiments.

Network. We modify SongUNet provided at <https://github.com/NVlabs/edm> to accept two time conditions t and s by using two time embedding layers.

ODE Solver. We use the second order Heun solver to calculate $\mathcal{L}_{\text{GCTM}}(\theta)$.

Gaussian perturbation. We apply a Gaussian perturbation from a normal distribution multiplied by 0.05 to sample \mathbf{x}_1 , excluding inpainting task.

A.2 EVALUATION

In this section, we describe the details of the evaluation to ensure reproducibility of our experiments.

Datasets. In unconditional generation task, we compare our GCTM generation performance using CIFAR10 training dataset. In image-to-image translation task, we evaluate the performance of models using test sets of Edges→Shoes, Night→Day, Facades from Pix2Pix. In image restoration task, we use FFHQ and apply following corruption operators H from I²SB to obtain measurement: bicubic super-resolution with a factor of 2, Gaussian deblurring with $\sigma = 0.8$, and center inpainting with Gaussian. We then assess model performance using test dataset.

Baselines. In image-to-image translation task, we compare three baselines: Pix2Pix from <https://github.com/junyanz/pytorch-CycleGAN-and-pix2pix>, Palette model from <https://github.com/Janspiry/Palette-Image-to-Image-Diffusion-Models>, and I²SB from <https://github.com/NVlabs/I2SB>. We modify the image resolution to 64×64 and keep the hyperparameters as described in their code bases, except that Pix2Pix due to the input size constraints of the discriminator. Same configuration is used in supervised image restoration task.

Metrics details. We calculate FID using <https://github.com/mseitzer/pytorch-fid> and IS from <https://github.com/pytorch/vision/blob/main/torchvision/models/inception.py>. We assess LPIPS from <https://github.com/richzhang/PerceptualSimilarity> with AlexNet version 0.1. In generation task, we employ the entire training dataset to obtain FID scores, and in the other task, we sample 5,000 test datasets. To obtain PSNR and SSIM, we convert the data type of model output to `uint8` and normalize it. We use <https://github.com/scikit-image/scikit-image> for PSNR and SSIM.

Sampling time. To compare inference speed, we measure the average time between the model taking in one batch size as input and outputting it.

B ALGORITHMS

B.1 OPTIMAL TRANSPORT

Algorithm 3 Sinkhorn-Knopp (SK)

- 1: **Input:** $\{\mathbf{x}_0^m\}_{m=1}^M, \{\mathbf{x}_1^m\}_{m=1}^M, \tau$
 - 2: Compute cost matrix $\mathbf{C} \in \mathbb{R}^{M \times M}$ such that $C_{i,j} = \|\mathbf{x}_0^i - \mathbf{x}_1^j\|_2^2$
 - 3: With Alg. 1 in (Cuturi, 2013), solve $\mathbf{P}^{\text{OT}} = \arg \min_{\mathbf{P}} \langle \mathbf{P}, \mathbf{C} \rangle - \tau H(\mathbf{P})$ s.t. $\mathbf{P}\mathbf{1} = \mathbf{P}^\top \mathbf{1} = \frac{1}{n}\mathbf{1}$
 - 4: Treat \mathbf{P}^{OT} as a discrete distribution over $\{1, \dots, M\} \times \{1, \dots, M\}$
 - 5: Sample $\{(i^m, j^m)\}_{m=1}^M \sim \mathbf{P}^{\text{OT}}$
 - 6: **Return:** $\{(\mathbf{x}_0^{i^m}, \mathbf{x}_1^{j^m})\}_{m=1}^M$
-

B.2 IMAGE RESTORATION

Algorithm 4 Zero-shot Image Restoration

- 1: **Input:** Measurement \mathbf{x}_1 , corruption \mathbf{H} , discretization $\{t_i\}_{i=0}^M$
 - 2: $\mathbf{x}'_{t_M} \sim \mathcal{N}(0, \mathbf{I})$
 - 3: **for** $i = M$ **to** 1 **do**
 - 4: $\boldsymbol{\epsilon} \sim \mathcal{N}(0, \mathbf{I})$
 - 5: **if** Method is DPS **then**
 - 6: $\hat{\mathbf{x}}_0 = g_\theta(\mathbf{x}'_{t_i}, t_i, t_i)$
 - 7: $\mathbf{x}'_{t_{i-1}} = (1 - t_{i-1})\hat{\mathbf{x}}_0 + t_{i-1}\boldsymbol{\epsilon}$
 - 8: **else if** Method is CM **then**
 - 9: $\hat{\mathbf{x}}_0 = G_\theta(\mathbf{x}'_{t_i}, t_i, 0)$
 - 10: $\mathbf{x}'_{t_{i-1}} = (1 - t_{i-1})\hat{\mathbf{x}}_0 + t_{i-1}\boldsymbol{\epsilon}$
 - 11: **else if** Method is GCTM **then**
 - 12: Evaluate score and ODE endpoint in parallel by $t = (t_i, t_i), s = (t_i, 0)$:
 - 13: $\tilde{\mathbf{x}}_0, \hat{\mathbf{x}}_0 = g_\theta(\mathbf{x}'_{t_i}, t_i, t_i), G_\theta(\mathbf{x}'_{t_i}, t_i, 0)$
 - 14: $\mathbf{x}'_{t_{i-1}} = (1 - t_{i-1})\tilde{\mathbf{x}}_0 + t_{i-1}\boldsymbol{\epsilon}$
 - 15: **end if**
 - 16: $\mathbf{x}'_{t_{i-1}} \leftarrow \mathbf{x}'_{t_{i-1}} - \lambda \nabla_{\mathbf{x}'_{t_i}} \|\mathbf{x}_1 - \mathbf{H}\hat{\mathbf{x}}_0\|_2^2$
 - 17: **end for**
 - 18: **Return:** \mathbf{x}'_0
-

In Alg. 4, we describe three zero-shot image restoration algorithms, DPS, CM, and GCTM. DPS uses the posterior mean $\mathbb{E}_{q(\mathbf{x}_0|\mathbf{x}'_{t_i})}[\mathbf{x}_0]$ to both traverse to a smaller time t_{i-1} and to approximate measurement inconsistency. As the posterior mean generally do not lie in the data domain, using it to calculate measurement inconsistency can be problematic. Indeed, approximation error in DPS is closely related to the discrepancy between the posterior mean and $\mathbf{x}'_{t_i \rightarrow 0}$ (see Theorem 1 in (Chung et al., 2022) for a formal statement). On the other hand, CM uses the ODE terminal point $\mathbf{x}'_{t_i \rightarrow 0}$ to traverse to a smaller time t_{i-1} and to approximate measurement inconsistency. While CM can have better guidance gradients as $\mathbf{x}'_{t_i \rightarrow 0}$ lie within the data domain, using $\mathbf{x}'_{t_i \rightarrow 0}$ to traverse to t_{i-1} can accumulate truncation error and degrade sample quality. For instance, see Figure 9 (a) in (Kim et al., 2024b). GCTM mitigates both problems by enabling parallel evaluation of posterior mean and ODE endpoint, as shown in Line 12-13 of Alg. 4.

B.3 IMAGE EDITING

Algorithm 5 Image Editing

- 1: **Input:** $(\mathbf{x}_0, \mathbf{x}_1) \sim q(\mathbf{x}_0, \mathbf{x}_1), t$
 - 2: $\hat{\mathbf{x}}_t = (1 - t)\text{Edit}(\mathbf{x}_0) + t\mathbf{x}_1$
 - 3: **Return:** $G_\theta(\hat{\mathbf{x}}_t, t, 0)$
-

C PROOFS

C.1 PROOF OF THEOREM 1

Proof. We observe that the velocity term in (12) may be expressed as

$$\mathbb{E}_{q(\mathbf{x}_0, \mathbf{x}_1 | \mathbf{x}_t)}[\mathbf{x}_1 - \mathbf{x}_0] = \mathbb{E}_{q(\mathbf{x}_0, \mathbf{x}_1 | \mathbf{x}_t)}[(\mathbf{x}_t - \mathbf{x}_0)/t] \quad (34)$$

$$= \mathbb{E}_{q(\mathbf{x}_0 | \mathbf{x}_t)}[(\mathbf{x}_t - \mathbf{x}_0)/t] \quad (35)$$

$$= (\mathbf{x}_t - \mathbb{E}_{q(\mathbf{x}_0 | \mathbf{x}_t)}[\mathbf{x}_0])/t \quad (36)$$

since \mathbf{x}_1 is determined given \mathbf{x}_0 and \mathbf{x}_t . This shows the equivalence between (12) and (14). Eqs. (15) and (16) are straightforward consequences of the equivalence between ODEs. \square

C.2 PROOF OF THEOREM 2

C.2.1 PROOF OF PART (I)

Proof. We first show equivalence of scores. We note that

$$\mathbf{x}_t \mapsto \bar{\mathbf{x}}_{t'} \quad (37)$$

is a bijective transformation, so by change of variables,

$$q(\bar{\mathbf{x}}_{t'} | \mathbf{x}_0) = (1+t) \cdot \mathcal{N}(\mathbf{x}_t | \mathbf{x}_0, t\mathbf{I}) = (1+t) \cdot p(\mathbf{x}_t | \mathbf{x}_0) \quad (38)$$

and marginalizing out \mathbf{x}_0 , we get

$$q(\bar{\mathbf{x}}_{t'}) = (1+t) \cdot p(\mathbf{x}_t). \quad (39)$$

It follows by Bayes' rule that

$$p(\mathbf{x}_0 | \mathbf{x}_t) = \frac{p(\mathbf{x}_t | \mathbf{x}_0)p(\mathbf{x}_0)}{p(\mathbf{x}_t)} \quad (40)$$

$$= \frac{(1+t)^{-1}q(\bar{\mathbf{x}}_{t'} | \mathbf{x}_0)q(\mathbf{x}_0)}{(1+t)^{-1}q(\bar{\mathbf{x}}_{t'})} \quad (41)$$

$$= \frac{q(\bar{\mathbf{x}}_{t'} | \mathbf{x}_0)q(\mathbf{x}_0)}{q(\bar{\mathbf{x}}_{t'})} \quad (42)$$

$$= q(\mathbf{x}_0 | \bar{\mathbf{x}}_{t'}) \quad (43)$$

and thus

$$\mathbb{E}_{p(\mathbf{x}_0 | \mathbf{x}_t)}[\mathbf{x}_0] = \mathbb{E}_{q(\mathbf{x}_0 | \bar{\mathbf{x}}_{t'})}[\mathbf{x}_0]. \quad (44)$$

for all $t \in (0, \infty)$ and \mathbf{x}_t . We now show equivalence of ODEs. Let us first re-state the diffusion PFODE below.

$$d\mathbf{x}_t = \frac{\mathbf{x}_t - \mathbb{E}_{p(\mathbf{x}_0 | \mathbf{x}_t)}[\mathbf{x}_0]}{t} dt. \quad (45)$$

With the change of variable

$$\bar{\mathbf{x}}_t = \mathbf{x}_t / (1+t), \quad (46)$$

we have

$$d\bar{\mathbf{x}}_t = -\frac{\mathbf{x}_t}{(1+t)^2} dt + \frac{1}{1+t} d\mathbf{x}_t \quad (47)$$

$$= -\frac{\mathbf{x}_t}{(1+t)^2} dt + \frac{\mathbf{x}_t - \mathbb{E}_{p(\mathbf{x}_0 | \mathbf{x}_t)}[\mathbf{x}_0]}{t(1+t)} dt \quad (48)$$

$$= -\frac{\bar{\mathbf{x}}_t}{1+t} dt + \frac{(1+t)\bar{\mathbf{x}}_t - \mathbb{E}_{p(\mathbf{x}_0 | \mathbf{x}_t)}[\mathbf{x}_0]}{t(1+t)} dt \quad (49)$$

$$= \frac{\bar{\mathbf{x}}_t - \mathbb{E}_{p(\mathbf{x}_0 | \mathbf{x}_t)}[\mathbf{x}_0]}{t(1+t)} dt \quad (50)$$

$$= \frac{\bar{\mathbf{x}}_t - \mathbb{E}_{q(\mathbf{x}_0 | \bar{\mathbf{x}}_{t'})}[\mathbf{x}_0]}{t(1+t)} dt \quad (51)$$

where we have used equivalence of scores at the last line. We then make the change of time variable

$$t' = t/(1+t) \implies dt' = \frac{1}{(1+t)^2} dt \quad (52)$$

which gives us

$$d\bar{\mathbf{x}}_{t'} = \frac{\bar{\mathbf{x}}_{t'} - \mathbb{E}_{q(\mathbf{x}_0|\bar{\mathbf{x}}_{t'})}[\mathbf{x}_0]}{t/(1+t)} dt' \quad (53)$$

$$= \frac{\bar{\mathbf{x}}_{t'} - \mathbb{E}_{q(\mathbf{x}_0|\bar{\mathbf{x}}_{t'})}[\mathbf{x}_0]}{t'} dt'. \quad (54)$$

This concludes the proof. \square

C.2.2 PROOF OF PART (II)

Proof. For the first equality in (22), transform PFODE variables (\mathbf{x}_t, t) into FM ODE variables $(\bar{\mathbf{x}}_{t'}, t')$ with (19), transport $\bar{\mathbf{x}}_{t'}$ to $\bar{\mathbf{x}}_{s'}$ with G_{GCTM} , and then transform FM ODE variables $(\bar{\mathbf{x}}_{s'}, s')$ into PFODE variables (\mathbf{x}_s, s) with the inverse of (19). Second equality in (22) follows directly from (20). \square

D LIMITATION, SOCIAL IMPACTS, AND REPRODUCIBILITY

Limitations. GCTMs are yet unable to reach state-of-the-art unconditional generative performance. We speculate further tuning of hyper-parameters in the manner of iCMs could improve the performance, and leave this for future work.

Social impacts. GCTM generalizes CTM to achieve fast translation between any two distributions. Hence, GCTM may be used for beneficial purposes, such as fast medical image restoration. However, GCTM may also be used for malicious purposes, such as generation of malicious images, and this must be regulated.

Reproducibility. We will open-source our code upon acceptance. Moreover, we have submitted experiment codes as a supplementary material.

E ADDITIONAL EXPERIMENTS

E.1 COMPARING I2I PERFORMANCE WITH OTHER BASELINE MODELS

We compare the image-to-image (I2I) performance of our model with two baseline approaches: EGSDE (Zhao et al., 2022) and BBDM (Li et al., 2023). Since BBDM, an I2I framework based on the Brownian Bridge process, leverages a latent diffusion model, we train it with a pixel-space diffusion model for a fair comparison. Both BBDM and EGSDE are trained on the Edges→Shoes dataset. As shown in Table 4, our GCTM outperforms all baselines across various metrics, even when evaluated with fewer sampling steps.

In addition, we visualize the image editing results in Fig. 9. While EGSDE generates realistic images, it fails to faithfully preserve the given conditions. BBDM, on the other hand, struggles to perform robustly on (unseen) conditional images. In contrast, GCTM produces realistic images while accurately maintaining the original conditions.

Table 4: Evaluation of I2I translation on Edges→Shoes with other baselines.

Method	NFE	Time (ms)	FID ↓	IS ↑	LPIPS ↓
BBDM (Li et al., 2023)	5	75	43.7	3.43	0.099
EGSDE (Zhao et al., 2022)	500	2590	198.1	2.87	0.476
GCTM	1	87	40.3	3.54	0.097

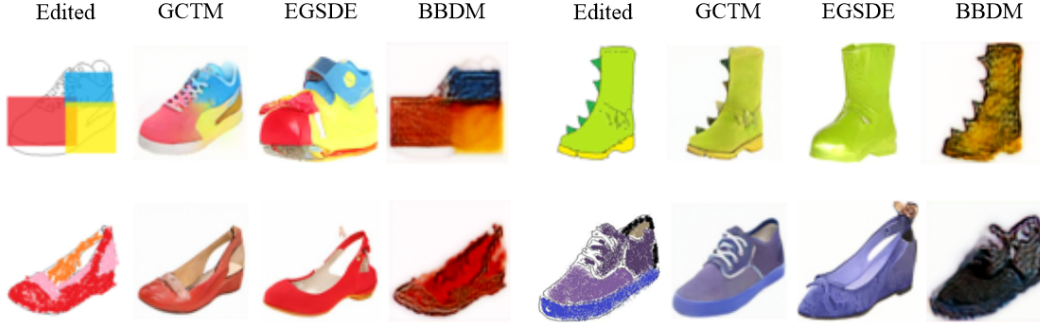


Figure 9: Comparison on image editing with GCTM and other baselines

E.2 CONTROLLABLE IMAGE EDITING

In this section, we demonstrate that effectiveness of image editing can be controlled. In Algorithm 5, we control the time point t to determine how much of the edited image to reflect. In Fig. 10, the results visualize how t effect the output of model output. We observe that the larger t , the more realistic the image, and the smaller t , the more faithful the edit feature. We set $t = 0.95$ and $t = 0.4$ at supervised coupling and independent coupling, respectively.

Figure 10: Controllability of image editing by t .

E.3 HIGH-RESOLUTION IMAGE RESTORATION

In Table 5, we demonstrate image restoration task of GCTM on ImageNet with higher resolution.

Table 5: GCTM evaluation of image restoration on ImageNet with 256×256 resolution.

Method	NFE	SR4 - Bicubic			Deblur - Gaussian			Inpaint - Center		
		PSNR \uparrow	SSIM \uparrow	LPIPS \downarrow	PSNR \uparrow	SSIM \uparrow	LPIPS \downarrow	PSNR \uparrow	SSIM \uparrow	LPIPS \downarrow
Corrupt	-	24.48	0.708	0.340	25.26	0.830	0.223	12.92	0.708	0.598
GCTM	1	26.70	0.771	0.223	34.65	0.948	0.032	21.56	0.808	0.229

E.4 ADDITIONAL IMAGE-TO-IMAGE TRANSLATION SAMPLES

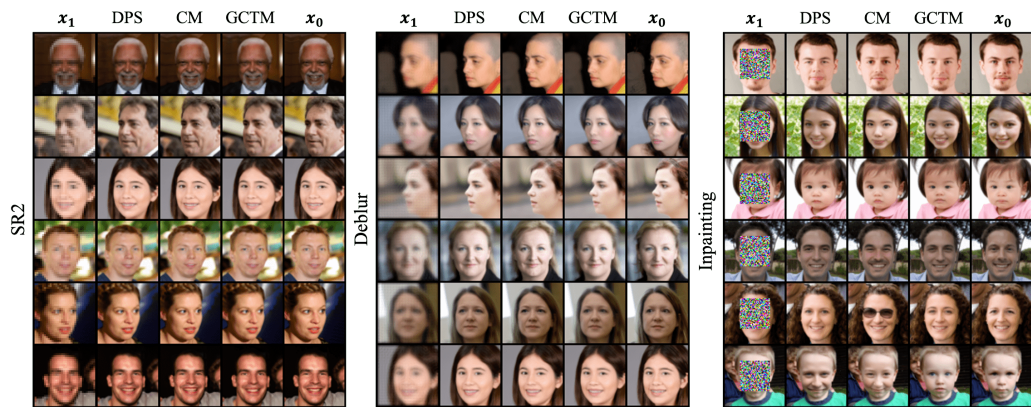


Figure 11: Additional results on image-to-image translation task on Edges→Shoes (top), Night→Day (middle) and Facades (bottom).

E.5 ADDITIONAL IMAGE RESTORATION SAMPLES



Figure 12: Additional results of supervised image restoration task on FFHQ 64×64 .

Figure 13: Additional results of zero-shot image restoration task on FFHQ 64×64 .Figure 14: Qualitative comparison of zero-shot algorithms on FFHQ 64×64 .